iScience

CellPress
OPEN ACCESS

Article

The pivotal role of bromine in FeMnKBr/Y_{Na} catalyst for CO_2 hydrogenation to light olefins

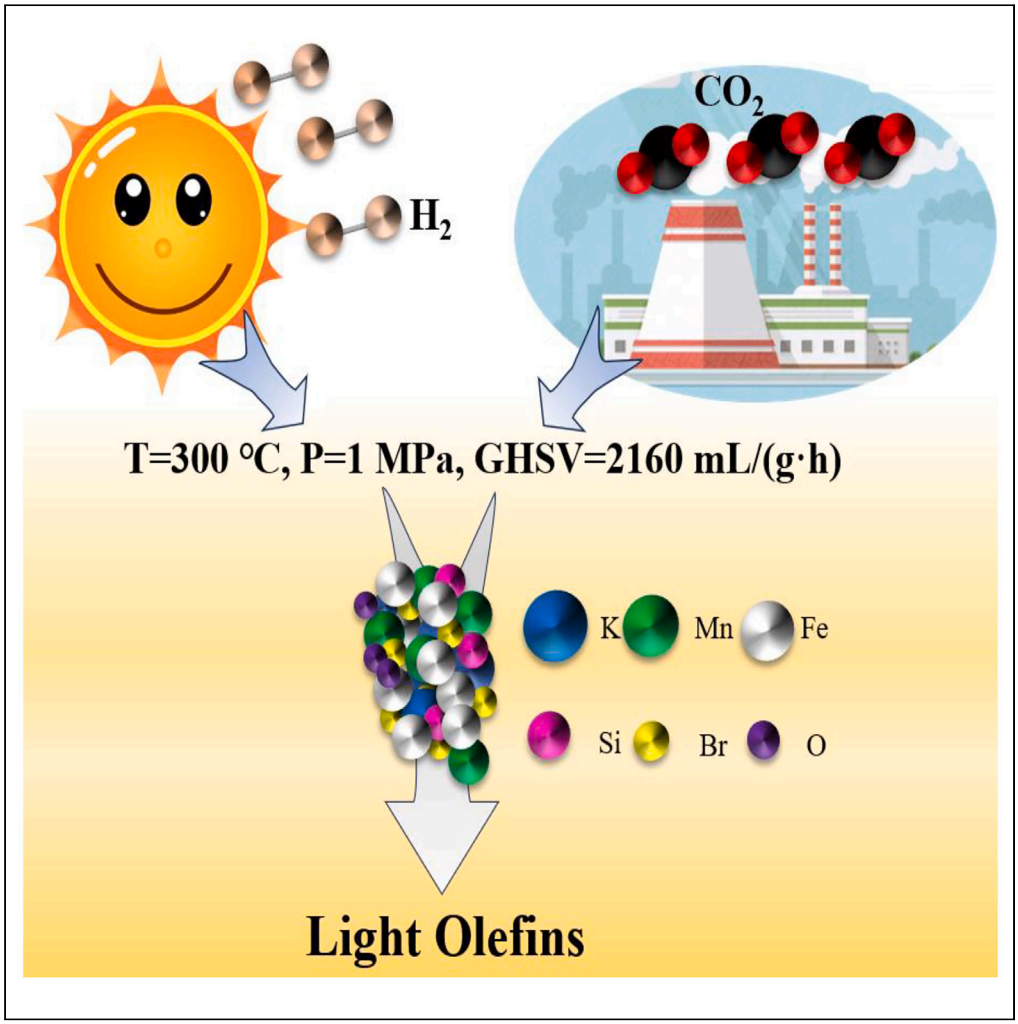

Wenjie Cui, Yudong Xia, Peipei Zhang, Yajie Fu, Xue Ye, Jie Li, Li Tan

yexue@yzu.edu.cn (X.Y.)
jieli@yzu.edu.cn (J.L.)
tan@fzu.edu.cn (L.T.)

Highlights

Br in FeMnKBr/Y_{Na} catalyst boosts CO_2 to light olefin conversion

The addition of Br breaks the traditional view of halogen toxicity

Br promotes the reduction and dispersion of the iron phase

The electronegativity of Br reduces the effect of K on catalysts

Cui et al., iScience *27*, 109621
May 17, 2024
https://doi.org/10.1016/j.isci.2024.109621

iScience

CellPress
OPEN ACCESS

Article

The pivotal role of bromine in FeMnKBr/Y_{Na} catalyst for CO_2 hydrogenation to light olefins

Wenjie Cui,[1] Yudong Xia,[1] Peipei Zhang,[2] Yajie Fu,[3] Xue Ye,[1,*] Jie Li,[1,*] and Li Tan[3,4,*]

SUMMARY

Light olefins are key intermediates in the synthesis of petrochemicals, and the conversion of stabilized carbon dioxide to light olefins using catalysts containing halogenated elements such as chlorine is a major challenge. Building on previous reports emphasizing the toxic effects of halogen elements on catalysts, we present the synthesis of FeMnKBr/Y_{Na} catalysts. This involved the synthesis of the catalyst by melt permeation using Br-containing potassium salts, other metal nitrates and Y_{Na} zeolites. The catalyst performed well in converting syngas (H_2/CO_2 = 3) to light olefins with a selectivity of 56.2%, CO_2 conversion of 34.4%, and CO selectivity of 13.6%. Adding Br aids in reducing the Fe phase, boosts catalyst carburization, and produces more iron carbide species. It also moderately deposits carbon on the active center's surface, enhancing active phase dispersion. Br's electronegativity mitigates the influence of K, reducing catalyst's carbon-carbon coupling ability, leading to more low-carbon olefins generation.

INTRODUCTION

Light olefins are crucial precursors in the chemical industry, underpinning the synthesis of various chemicals, including polymers, explosives, and other organic compounds. The current methodologies for producing light olefins hold considerable significance. Despite the global recognition of petroleum cracking route as a prevalent method, the petroleum, a non-renewable resource, coupled with its increasing environmental impact, underscores the imperative need for new technologies and the selection of alternative feedstocks to synthesize light olefins more securely, efficiently, and sustainably.[1–3]

Fischer-Tropsch synthesis (FTS) emerges as a promising alternative, utilizing CO or CO_2 as feedstocks and undergoes multiphase hydrogenation reactions under catalyzed to yield hydrocarbon products with a wide carbon number distribution.[4–11]

Preliminary studies have been conducted on the direct conversion of CO_2 to light olefins. Iron-based catalysts have been extensively studied for their cost-effectiveness, sensitivity to the H_2/CO_2 ratio, and capacity for selective generation of diverse products under conditions suitable for FTS. Research indicates that the introduction of promoter elements can enhance catalytic efficiency, while also allowing for precise modulation of product yield.[12] Previous studies have reported that potassium salts with different anions exhibit the presence of K_2CO_3 under various conditions, but the effect on catalytic performance is different.[13–15] The type of anion notably affects the catalytic activity and product distribution. Sulfates, for instance, do not promote the formation of iron carbide on Fe catalysts, thereby diminishing CO_2 hydrogenation efficiency. In contrast, direct application of K_2CO_3 increases interaction with iron carbide, facilitating the formation of more iron carbide species and altering surface alkalinity, which in turn augments catalytic performance. The reduced catalysts reveal the formation of potassium bicarbonate from KOH or K_2CO_3, resulting in an increase in methane production at low temperatures, [16–18] though this does not impact catalytic activity.[19–21] Contrastingly, KCl reduces surface alkalinity, favoring carbon chain growth, yet its limited surface alkalinity precludes adequate CO_2 adsorption for forming more iron carbide, deviated from the results obtained with other potassium salts. Some studies argue that the addition of a small amount of chlorine additions to the catalyst can synergistically interact with CO_2, inhibit the adsorption of H on active sites, alter surface C/H ratio, thus improving the selectivity of low-carbon olefins.[22–30] On the other hand, the effect of Br, another halogen, on iron-based catalysts remains less understood.

Despite this, previous reports have largely overlooked metal salts containing halogen elements, given the prevailing view of halogen elements as catalyst-toxic substances.[31,32] The specific role of Br elements is yet to be fully elucidated. In this study, we present the synthesis of FeMnK/Y_{Na} catalysts prepared with potassium salts containing different anions. Detailed characterization and theoretical investigations were conducted. Among them, the FeMnKBr/Y_{Na} catalyst exhibited optimal catalytic performance. Under conditions of T = 300°C, p = 1 MPa, H_2/CO_2 = 3, and GHSV = 2160 mL g^{-1} h^{-1}, the selectivity for low carbon olefins in hydrocarbon products reached 56.4%, with a carbon dioxide conversion rate of 34.4%.

[1]School of Chemistry and Chemical Engineering, Yangzhou University, Yangzhou 225002, China
[2]CNOOC Institute of Chemicals & Advanced Materials, Beijing 102209, China
[3]Fujian Key Laboratory of Electrochemical Energy Storage Materials, State Key Laboratory of Photocatalysis on Energy and Environment, College of Chemistry, Fuzhou University, Fuzhou 350108, China
[4]Lead contact
*Correspondence: yexue@yzu.edu.cn (X.Y.), jieli@yzu.edu.cn (J.L.), tan@fzu.edu.cn (L.T.)
https://doi.org/10.1016/j.isci.2024.109621

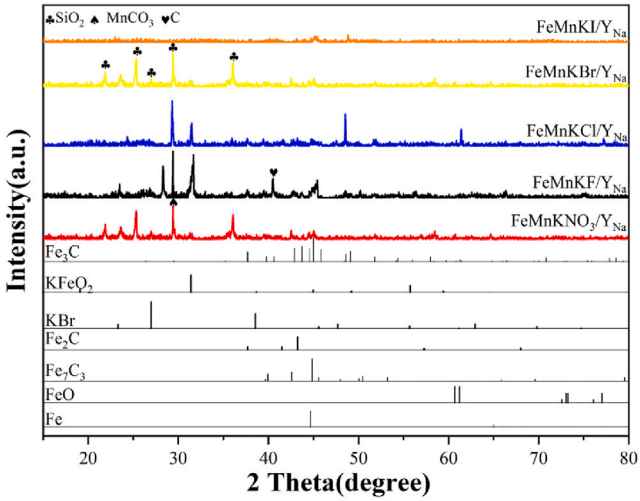

Figure 1. XRD analysis of the different carburized catalysts

RESULTS AND DISCUSSION

The structural and morphological characterization of the catalysts

We investigated the phase composition of catalysts after calcination. As depicted in Figure S1, it was observed that catalysts prepared with different potassium salts showed similar iron phase compositions post-calcination, predominantly existing as Fe_2O_3. This uniformity in the iron phase was notable across all samples. However, a divergence was observed in the form of the K promoter. In FeMnKI/Y_{Na}, K was uniquely retained in the form of KI, contrasting with the other catalysts where potassium was present in the forms of K_2CO_3 and KFe_2O_2 (Figure S1). The characteristic peaks at 31.6° and 44.8° are attributed to K_2CO_3 (110) and K_2CO_3 (202), and the 31.4° characteristic peak is attributed to $KFeO_2$ (220).[33] This variation in the potassium form highlights the impact of different potassium salts on the chemical structure and potentially on the catalytic properties of the synthesized materials.

As all we know, zero-valent iron is often recognized as the active center of reverse water-gas shift (RWGS), Fe_7C_3 is the active center of FTS, although its reactivity is poorer than that of Fe_5C_2 and Fe_2C. To investigate the composition of the active phase in our catalysts, we conducted X-ray diffraction (XRD) analysis on the carburized catalysts (Figure 1). 31.36° of the characteristic peaks are attributed to $MnCO_3$ (106), 44.99° of the characteristic peaks are attributed to Fe_3C (031), 42.3° of the characteristic peaks are attributed to Fe_2C (101), 44.85° of the characteristic peaks are attributed to Fe_7C_3 (211), 61.24° and 77.05° of the characteristic peaks are attributed to the 110 and 202 crystal planes of FeO, 44.67° of the characteristic peaks are attributed to Fe (110). The results showed that different phases-Fe, Fe_3C_7, FeO, Fe_3C, and Fe_2C are present in the catalysts after carburized with CO. More zero-valent iron is present in FeMnKNO$_3$/Y_{Na}, but fewer iron carbide species are present. FeMnKF/Y_{Na}, FeMnKCl/Y_{Na}, FeMnKBr/Y_{Na}, and FeMnKI/Y_{Na} all contain Fe_3C_7 and Fe_2C. In addition, FeMnKCl/Y_{Na} also contains a small amount of FeO, and at the same time, we found that the $KFeO_2$ phase is still retained in this catalyst. Differences in the iron phases show the effect of different anions on the catalyst structure and thus on the catalyst performance.

The SEM images of the FeMnKBr/YNa as a sample catalyst after the reaction exhibited a morphology characterized by a dense block-like structure formed by layer stacking, and the morphology of the YNa molecular sieve was no longer perceptible (Figures 2A and 2B). This structural transformation can be ascribed to the perturbation experienced by the molecular sieve during the catalyst preparation phase, a finding that aligns with the XRD results (Figure S2). In Figure S3, it is observed that despite the disruption of the molecular sieve structure, and the catalyst retains the acidic sites of the molecular sieves. In addition, the *in-situ* growth of carbon on the catalyst surface was promoted during the reaction in CO and CO2 atmospheres. This phenomenon was accompanied by a relatively high degree of carbon deposition, indicative of the dynamic interactions occurring at the catalyst surface during the reaction, and potentially influencing the catalyst's activity and selectivity.

For more detail morphology characterization, we employed TEM to examine the extent of carbon deposition on the catalyst surfaces post-carburization. The transmission electron microscopy (TEM) images clearly demonstrated that various catalysts, upon carburization in CO atmosphere, undergo *in-situ* carbon deposition or nanotube growth on their surfaces (Figures 2E–2H). Catalysts employing traditional potassium nitrate displayed substantial uneven carbon deposition (Figure 2E). In contrast, catalysts containing different halogen elements exhibited variations in carbon deposition. Consequently, smooth and uniformly coated carbon developed on the surfaces of the active phase. Conversely, catalysts like FeMnKCl/Y_{Na} (Figure 2G) and FeMnKI/Y_{Na} (Figure 2H) demonstrated the growth of carbon nanotubes. In the case of FeMnKBr/Y_{Na}, there was a uniform growth of carbon deposition without significant aggregation (Figure 2C). The moderate degree of carbon deposition maintains the catalyst's high activity, simultaneously reducing CO selectivity and further enhancing CO_2 conversion to low-carbon olefins.[34]

Post-reaction TEM analysis provided further insights. The FeMnKBr/Y_{Na} and FeMnKNO$_3$/Y_{Na} catalyst showed increased carbon deposition due to adsorbed CO_2 during the reaction (Figures 2D and 2I). The other three catalysts indicated of ongoing carbon nanotube formation. The morphology of carbon nanotubes on FeMnKF/Y_{Na}'s surface was disrupted, displaying a distinct shape from the carburized state, indicating

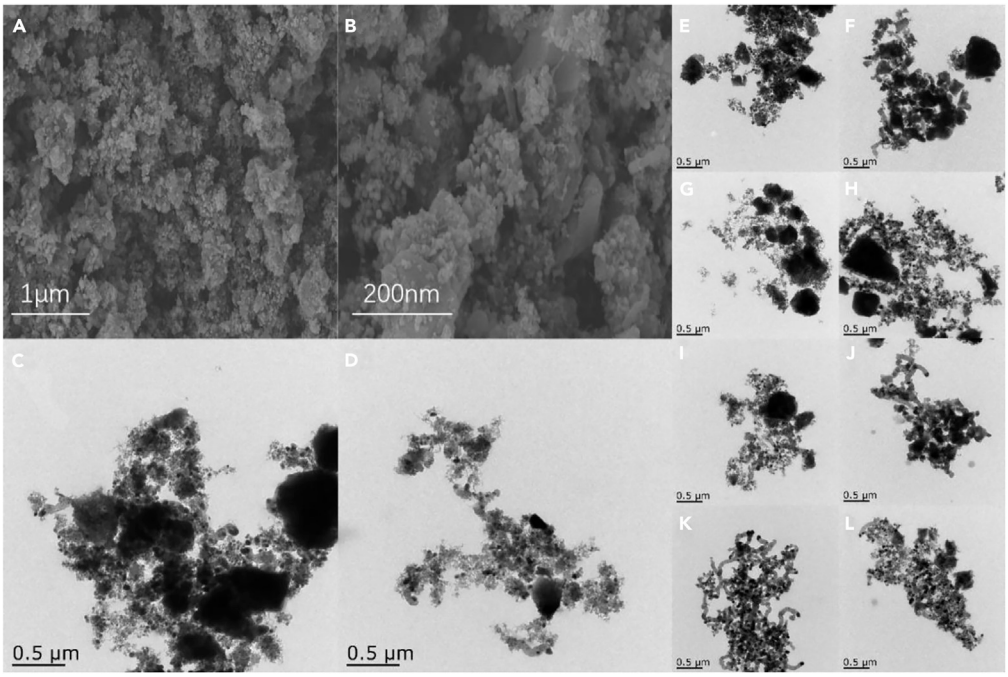

Figure 2. SEM and TEM of different post-carburizing and post-reaction catalysts

(A and B) SEM analysis of used FeMnKBr/Y_{Na} catalyst.

(C) TEM of the carburized FeMnKBr/Y_{Na} catalyst.

(D) TEM of the used FeMnKBr/Y_{Na} catalyst.

(E–H) TEM of the carburized catalysts: FeMnKNO_3/Y_{Na}; FeMnKF/Y_{Na}; FeMnKCl/Y_{Na}; FeMnKI/Y_{Na}.

(I–L) TEM of the used catalysts: FeMnKNO_3/Y_{Na}; FeMnKF/Y_{Na}; FeMnKCl/Y_{Na}; FeMnKI/Y_{Na}.

sintering during the reaction (Figure 2J). The surface of FeMnKCl/Y_{Na} displayed smoother, longer, and more numerous carbon nanotubes, uniformly wrapping around the active phase (Figure 2K). Also, TEM images revealed wider and more uniformly distributed carbon nanotubes on FeMnKI/Y_{Na} (Figure 2L). These findings underscore the intricate relationship between the catalyst composition, carbon deposition, and resultant structural changes, which are crucial for understanding catalyst performance in CO_2 hydrogenation to low-carbon olefins. The *in situ* grown carbon nanotubes on those halogen elements besides Br added catalysts are negative for CO_2 hydrogenation to low-carbon olefins according to the catalytic performance.

Building on our previous analysis, we further investigated the elemental distribution on the catalyst surface. Through EDX elemental diffraction tests, we observed that catalysts containing different potassium salts demonstrated a uniform dispersion of elements. The application of melt-infiltration method was in instrumental in facilitating the diffusion of more metal ions into the supporter's pores. However, it was noted that elements like Fe, Mn, K, and various halogens exhibited differing degrees of dispersion (Figures 3A–3D).

The pronounced dispersion of these elements is critical for ensuring that the catalyst's excellent catalytic activity. Specifically, the EDX results of the FeMnKBr/Y_{Na} catalyst clearly showed a superior dispersion of the iron phase compared to other catalysts. In other catalysts, the *in-situ* growth of carbon nanotubes on the iron phase surface during carburization and reaction led to an uneven dispersion of the active phases. In contrast, FeMnKBr/Y_{Na}, while also undergoing *in-situ* growth of carbon deposition, to some extent, carburized catalyst aggregation and sintering, promoting the even dispersion of active components. This process facilitated the even dispersion of active components, allowing the elements K, Mn, and Br to be uniformly dispersed around the active center. The presence of K played a pivotal role in regulating electron density and hydrogen density on the Fe phase surface. Additionally, K aided in the adsorption and dissociation of CO_2, thereby enhancing the catalyst's overall activity.[33–37] This mechanism is particularly beneficial in increasing the conversion of CO_2 into low-carbon olefins, while simultaneously reducing the selectivity of CO.

We employed various analytical techniques to quantify the Na, K, and anion concentrations within the catalyst, aiming to elucidate the influence of distinct elemental compositions on catalyst efficacy. As delineated in Table S1, deviations from theoretical expectations were observed for all halogens; notably, fluorine and iodine exhibited considerably low loadings, potentially attributable to their predisposition toward volatilization and subsequent loss during the calcination phase. In contrast, chlorine and bromine demonstrated enhanced stability and retention, manifesting in higher loadings. Examination of Table S2 revealed uniform sodium loadings across various catalyst formulations, derived partly from residual NaOH treatment and more partly from incorporation via molecular sieves. This uniformity suggests an intentional Na addition to the catalysts, functioning in concert with K to augment surface alkalinity and modulate the surface C/H ratio. Moreover, the

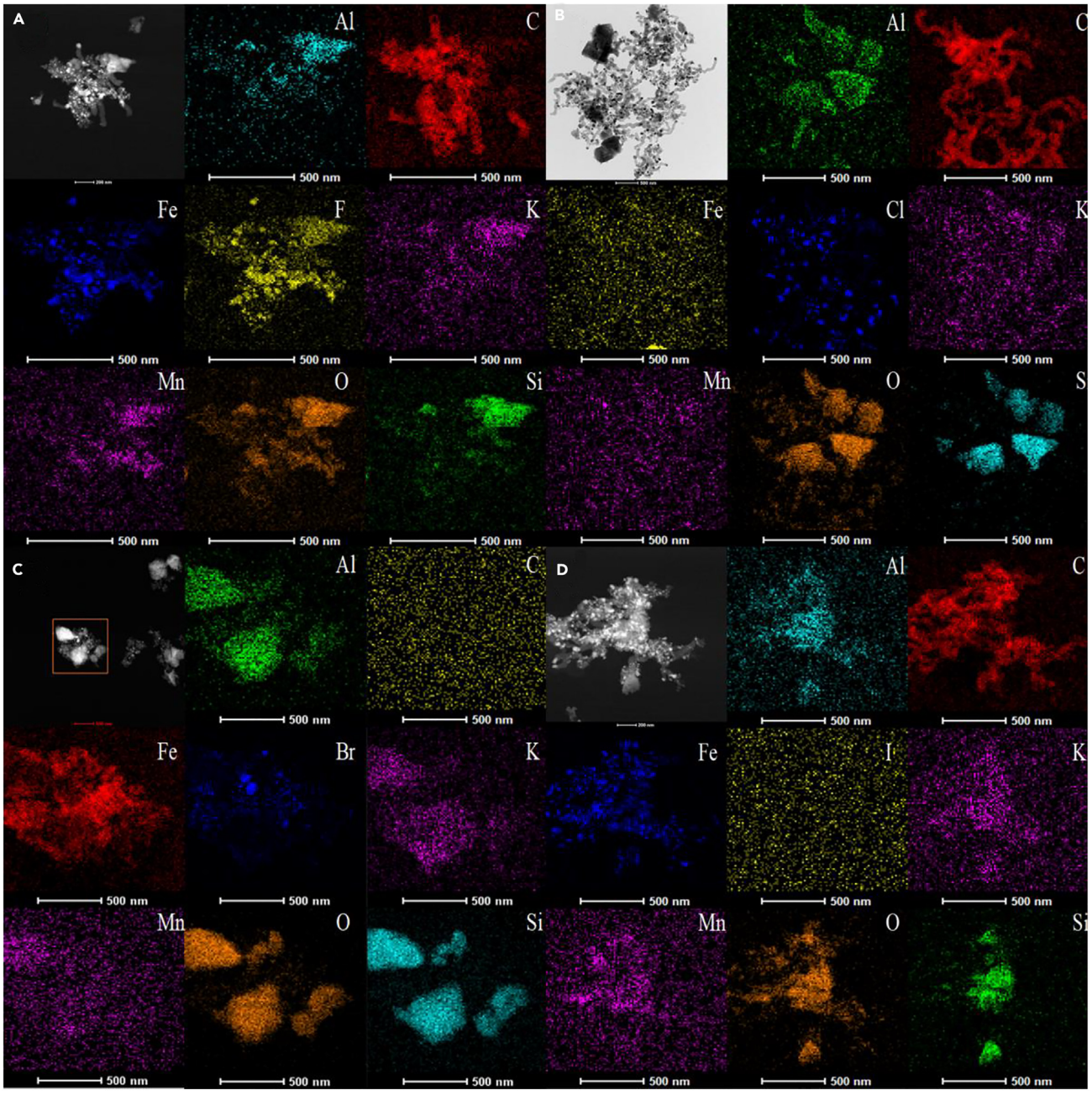

Figure 3. Element distribution on the catalyst surface after use

(A –D) EDX analysis of the used catalysts: FeMnKF/Y_{Na}; FeMnKCl/Y_{Na}; FeMnKBr/Y_{Na}; FeMnKI/Y_{Na}.

volatilization of fluorine potentially contributed to an elevated K proportion in the FeMnKF/Y_{Na} catalyst, while the K loadings in the other three catalysts remained relatively unchanged.

Continuing from the previous discussions, we delved deeper into the electronic information of the catalyst surface after carburization by conducting X-ray photoelectron spectroscopy (XPS) analyses (Figure 4). The XPS spectra of C 1s revealed the presence of carbon in the forms of C-C and C-O on the catalyst surface (Figure 4A). Regarding the composition of iron, on the FeMnKNO_3/Y_{Na} surface, there was a substantial presence of iron carbide species, while the contents of Fe^{2+} and Fe^{3+} were relatively low. After carburization, the surface iron on FeMnKF/Y_{Na}, FeMnKCl/Y_{Na}, and FeMnKI/Y_{Na} existed mainly in the forms of Fe^{2+}, Fe^{3+}, and Fe^0, consistent with the XRD results. In the case of FeMnKBr/Y_{Na}, an increase in Fe^0 and iron-carbon species was observed, coupled with a significantly decrease of Fe^{2+} and Fe^{3+}, with Fe^{3+} almost disappearing (Figure 4B). This suggests that the addition of Br is beneficial for Fe^{3+} reduction, which helps promote the catalytic performance.

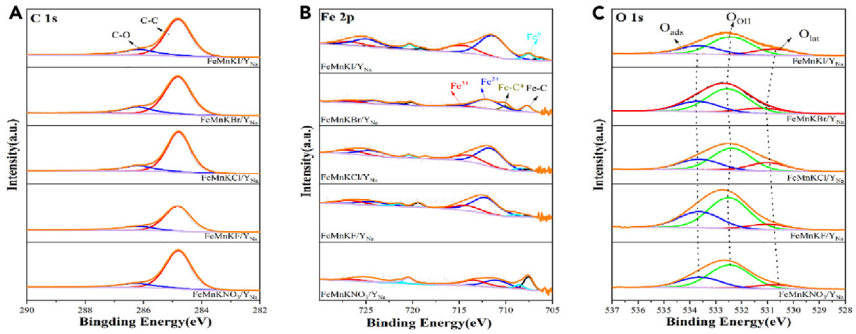

Figure 4. XPS analysis of the carburized catalysts
(A) C 1s, (B) Fe 2p, (C) O 1s.

There was also a significant difference in the presence of surface oxygen (Figure 4C). FeMnKF/Y_{Na} exhibited the highest O_{ads} characteristic peak. FeMnKCl/Y_{Na} and FeMnKI/Y_{Na} had higher O_{lat} content compared to FeMnKBr/Y_{Na}, indicating that Br promoted the reduction of the iron phase.

Furthermore, due to the different electronegativities of the halogens, there was a distinct shift in the iron binding energy (Figure 4B). In FeMnKBr/Y_{Na}, the iron binding energy shifted to a higher value, implying a lower electron availability for iron in this catalyst compared to others. K inhibits the adsorption of H on the surface by supplying electrons to the active center to increase the C/H ratio on the surface for C-C growth, [34,36,37] whereas Br reduces the electron density at the active center, achieving an optimal C/H ratio conductive to generating more CH_X fragments for low-carbon olefins production. This effect is not replicated with other halogens. Although in FeMnKCl/Y_{Na}, the lower binding energy of iron, the acquisition of more electrons and the control of the surface H density, which can inhibit the secondary hydrogenation of olefin. However, it is possible that its lower surface alkalinity or interaction with CO_2 prevents the adsorption of more CO_2 and the generation of more CH_x fragments, which in turn sustains the hydrogenation process and improves the selectivity of alkanes.[26] XPS analysis showed that oxygen adsorption at the same level as in the other catalysts promotes the continuation of the hydrogenation reaction and improves the selectivity of alkanes (Figure 4C).

Regarding the carburized catalyst, we also examined the presence of anions on the surface and found that F, Cl, and I were detected, while Br did not show characteristic peaks (Figures S6A, S4, and S5A), which suggests that the high degree of dispersion of Br or carbon deposition masked its signal. Meanwhile, the signal intensities of Cl and I decreased significantly after the reaction (Figures S5B and S6C), probably due to the masking of their signals by the carbon covering the surface. At the same time, there is not much difference between K and Mn on the surface after carburization, and different degrees of carbon build-up will change the characteristic peak intensities, but not the binding energy (Figure S7). Additionally, a comparison with XPS data after the reaction revealed no significant changes in carbon, no characteristic peaks of Fe, indicating an increased carbon deposition affecting the Fe signal value (Figure S8A). During the reaction, different degrees of carbon buildup occurred on the catalyst surface, so the characteristic peaks of K are somewhat different, but the binding energy of K was found not to be shifted from the figure, indicating its ability to provide electrons is consistent (Figure S8B). Regarding the way of existence of C on the surface after the reaction there is no obvious difference after the carburization (Figure S8C). Meanwhile, there was a corresponding decrease in the signal value for O (Figure S8D), further underscoring the complex interplay of elements on the catalyst surface and its impact on catalytic performance.

Raman spectroscopy was employed to evaluate the catalysts post-carburization and post-reaction, focusing on the extent of carbon deposition (Figure 5). The Raman spectroscopy results for the catalysts, both after carburization and subsequent reaction, demonstrated varying degrees of carbon deposition. Comparing the catalysts after carburization and reaction, all other catalysts exhibited D and G bands related to carbon. The D band at 1357.89 cm^{-1} indicates lattice carbon defects, while the G band at 1582.38 cm^{-1} reflects the degree of carbonization of the catalyst. After carburization and reaction, the catalyst with added K_2CO_3 showed no significant change in surface carbon deposition. However, the catalysts containing KF showed a significant decrease in the characteristic peaks related to C after the reaction, which could be attributed to its instability as well as the disruptive sintering of carbon nanotubes. The catalyst with KCl showed distinct characteristic peaks for carbon before and after the reaction. The increase in the intensity of the carbon characteristic peaks before and after the reaction for the catalysts containing KBr indicates an increase in the degree of surface carbon deposition, whereas the degree of surface carbon deposition decreases after the reaction for the catalysts containing KI.

This moderate surface carbon deposition is crucial as it fosters high dispersion of the active phase, which is instrumental in ensuring high conversion rates. Additionally, it facilitates the efficient conversion of CO_2 to low-carbon olefins. These findings underscore the significance of the specific potassium salt used in the catalyst formulation, as it directly impacts the carbon deposition and, consequently, the catalyst's overall performance in the conversion process.

To elucidate the influence of various anions on the catalyst's reduction behavior, H_2-TPR analyses were conducted, as depicted in Figure S9. The analyzed catalysts exhibited three distinct reduction peaks, correlating to the stepwise reduction from Fe_2O_3 to Fe_3O_4, Fe_3O_4 to FeO, and finally FeO to metallic Fe. The H_2-TPR profile of FeMnKNO$_3$/Y_{Na} catalyst presented a broad, indistinct peak, obscuring the

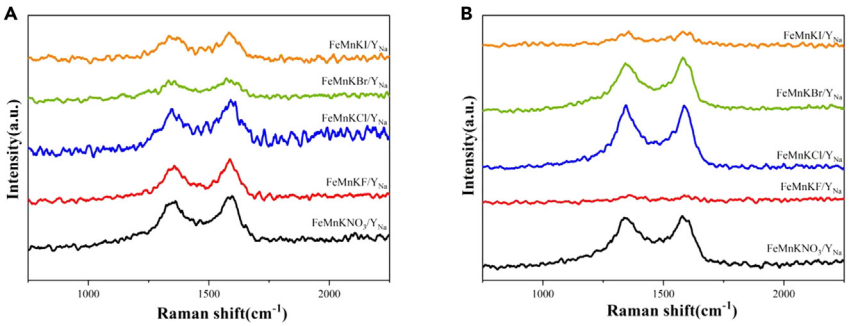

Figure 5. Comparison of carbon deposition of different catalysts after carburization and use

Raman plots of different catalysts: (A) carburized (B) used.

differentiation between the iron phases' reduction steps. Notably, for catalysts such as FeMnKBr/Y_{Na}, FeMnKF/Y_{Na}, and FeMnKCl/Y_{Na}, the peaks associated with the reduction from Fe_2O_3 to Fe_3O_4 and Fe_3O_4 to FeO shifted toward lower temperatures. This shift suggests that the incorporation of F, Cl, and Br anions enhances the reducibility of Fe_2O_3 and Fe_3O_4. However, F and I additions were found to impede the FeO to Fe transition, as evidenced by peak shifts to higher temperatures, whereas Cl and Br additions appeared to facilitate the reduction to metallic Fe, thereby promoting the formation of more Fe and subsequently more active iron carbide species with increased active sites.

CO-TPR was utilized to assess the impact of various anions on the catalyst's carburization potential. As shown in Figure S10, while the carburization temperatures remained similar across catalysts with different anions, the quantity of consumed CO varied significantly. Specifically, the introduction of Br markedly increased CO adsorption, thereby enhancing the catalyst's carburization efficiency and leading to the formation of a greater number of active iron carbide species, which in turn augmented the catalyst's performance.

Additionally, CO_2-TPD experiments were performed to evaluate the effects of anion variation on CO_2 adsorption characteristics of the carburized catalysts, detailed in Figure S11. Peaks around 150°C were attributed to physical CO_2 adsorption, those near 350°C to medium-strength adsorption, and peaks around 700°C to strong CO_2 adsorption. It was observed that the presence of different anions influenced both the weak and strong CO_2 adsorption capabilities, with F notably enhancing strong CO_2 adsorption. Conversely, the addition of Br eliminated strong adsorption peaks while significantly increasing medium-strength CO_2 adsorption. These findings underscore the significant impact of anions on CO_2 adsorption capacity, with medium-strength adsorption playing a pivotal role in modulating the catalyst's catalytic efficacy.

Catalytic performance for CO_2 hydrogenation

Table 1 presents a comprehensive summary of the performance metrics for various catalysts. Notably, FeMnKBr/Y_{Na} emerges as the standout catalyst, exhibiting the highest CO_2 conversion rate at 35.0%, the lowest CO selectivity at 13.2%, and the most significant selectivity for light olefins at 56.2%. In contrast, FeMnKF/Y_{Na} records the highest CO selectivity at 44.5%. Meanwhile, FeMnKCl/Y_{Na} demonstrates a notable preference for light alkanes with a selectivity of 44.5%. When compared to FeMnKBr/Y_{Na}, the catalysts FeMnKNO$_3$/Y_{Na}, FeMnK$_2$CO$_3$/Y_{Na}, and FeMnKI/Y_{Na} exhibit less impressive performance, with CO_2 conversion rates of 31.1%, 31.0%, and 29.2%, respectively. These data clearly highlights the superior efficacy of FeMnKBr/Y_{Na} in CO_2 conversion and selectivity toward desired products, setting it apart from its counterparts.

To elucidate the impact of halogen anions with differing electronegativities on catalyst performance, we conducted a series of performance tests. As depicted in Figure 6, both CO_2 conversion and CO selectivity exhibited a volcano-shaped trend, with FeMnKBr/Y_{Na} demonstrating the most optimal catalytic performance. Notably, XRD analysis revealed that FeMnKF/Y_{Na} still contained Fe^{3+} post-reduction. TEM and Raman spectroscopy analyses showed that the carbon nanotubes on the FeMnKF/Y_{Na} surface were disrupted. This led to reduced carbonation and significant sintering, suggesting that the active center underwent substantial oxidation. This condition likely resulted in the strongest RWGS reaction, culminating in the highest CO selectivity for FeMnKF/Y_{Na}. Comparatively, the CO_2 conversion and CO selectivity of FeMnKCl/Y_{Na} and FeMnKI/Y_{Na} did not show much variance. However, the product compositions varied and of all the catalysts, FeMnKCl/Y_{Na} had the highest low-carbon alkanes selectivity and the products were dominated by low-carbon alkanes. This over-hydrogenation behavior aligns with observations from XPS analysis. On the other hand, the products from FeMnKI/Y_{Na} maintained a high proportion of low-carbon olefins, yet these were still lower compared to FeMnKBr/Y_{Na}. Outstandingly, FeMnKBr/Y_{Na} achieved the best catalytic performance overall. It has the highest CO_2 conversion, the lowest CO selectivity, the highest low-carbon olefins selectivity, and the product is mainly low-carbon olefins. These findings underscore the significant influence of halogen anions on the catalytic behavior and highlight the exceptional efficiency of FeMnKBr/Y_{Na} in the conversion process, making it a highly effective catalyst for CO_2 hydrogenation to low-carbon olefins.

To further decipher the influence of anions on catalyst performance, we performed a series of experiments with different catalysts. The experiments affirmed that FeMnKBr/Y_{Na} exhibited superior catalytic performance at an optimal temperature of 300°C and pressure of 1 MPa. This catalyst demonstrated the lowest CO selectivity and the highest CO_2 conversion, as illustrated in Figure 7. The enhanced performance of FeMnKBr/Y_{Na} compared to FeMnKNO$_3$/Y_{Na} and FeMnK$_2$CO$_3$/Y_{Na} can be attributed to the role of Br. The introduction of Br was

Table 1. Performance testing table of FeMnK/Y_{Na} catalysts with different anions

Catalysts	CO_2 Con.(%)	CO Sel. (%)	STY (g $_{C2-C4}^{=}$ kg_{cat}^{-1} h^{-1})	Product selectivity (%)			
				CH_4	C_2-$C_4^{=}$	C_2-C_4^{0}	C_{5+}
FeMnKNO_3/Y_{Na}	31.1	19.7	27.7	31.3	36.2	17.0	15.6
FeMnK_2CO_3/Y_{Na}	31.0	19.0	41.1	29.2	42.6	12.8	15.4
FeMnKOH/Y_{Na}	31.0	19.2	38.2	32.3	40.1	18.1	9.5
FeMnKF/Y_{Na}	22.3	44.5	22.7	34.1	33.7	13.2	19.0
FeMnKCl/Y_{Na}	30.7	19.3	18.9	40.4	20.3	31.9	7.3
FeMnKBr/Y_{Na}	35.0	13.2	52.4	28.4	56.2	10.0	5.4
FeMnKI/Y_{Na}	29.2	21.7	33.3	31.9	36.9	17.3	13.9

Carburization condition: CO/N_2 = V(20%CO)/V(80%N_2), SV = 1200 mL g^{-1} h^{-1}, T = 440°C, p = 0.5 MPa, 8 h.
Reaction condition: H_2/CO_2 = 3, SV = 2160 mL g^{-1} h^{-1}, T = 300°C, p = 1.0 MPa.

observed to facilitate the reduction of the iron phase, leading to the generation of more iron carbide species with a higher number of active centers. This was substantiated by XRD and XPS analyses. Additionally, TEM investigations revealed that the presence of Br aids in the formation of more favorable carbon nanotube structures and induces moderate carbon deposition at the active centers. Consequently, FeMnKBr/Y_{Na} enhances the conversion of CO_2 to low-carbon olefins, while simultaneously inhibiting the RWGS reaction, thus producing less CO. At the same time, the hydrocarbon is mainly low-carbon olefins, and the content of C_{5+} is less. This is likely due to Br's electron-attracting capacity, which diminishes the influence of K and reduces the catalyst's carbon-carbon coupling ability. This electronic effect was further confirmed through XPS analysis. Performance tests clearly demonstrated that halogens with varying electronegativities exert different impacts on the catalysts. A suitable electronegativity can modify the effect of potassium, altering the catalyst's activity and selectivity profiles. These insights are crucial for understanding the nuanced roles of halogen anions in catalyst design, particularly in applications involving CO_2 hydrogenation to low-carbon olefins.

We conducted temperature gradient tests and pressure gradient tests to further understand the catalysts' performance dynamics (Figure 8). At a temperature of 280°C, both the selectivity of CO and C_{5+} was relatively high, while the selectivity of low carbon olefins was low, accompanied by a poor conversion rate. This phenomenon suggests that at this temperature, the RWGS reaction was intense, leading to the generation of a significant amount of CO. Additionally, the high degree of carbon-carbon coupling, enhancing the formation of longer chains, can be attributed to the electron-promoting effect of K.[36] At a higher temperature of 320°C, both the CO_2 conversion and CO selectivity were slightly lower compared to those at 300°C. It is noteworthy that the selectivity for methane decreased, but due to the strong influence of K,[37–39] there was still an improvement in the conversion of low-carbon olefins to C_{5+} (Figure S11A). In terms of pressure gradients, a similar trend was observed. The CO selectivity, CO_2 conversion rate, and selectivity for low-carbon olefins exhibited a volcano-shaped curve (Figure S11B). Based on these observations, we determined that the catalytic performance peaked at T = 300°C, p = 1 MPa, where the

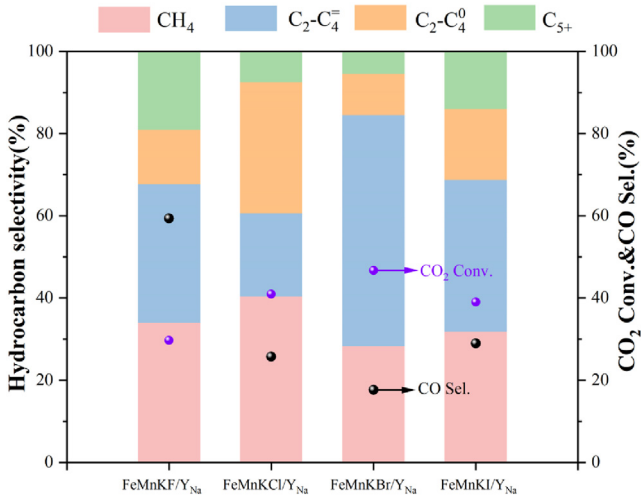

Figure 6. Catalytic performances for CO_2 hydrogenation over the halide-based FeMnK/Y_{Na} catalyst
Reaction conditions: T = 300°C, p = 1.0 MPa, SV = 2160 mL g^{-1} h^{-1}, H_2/CO_2 = 3.

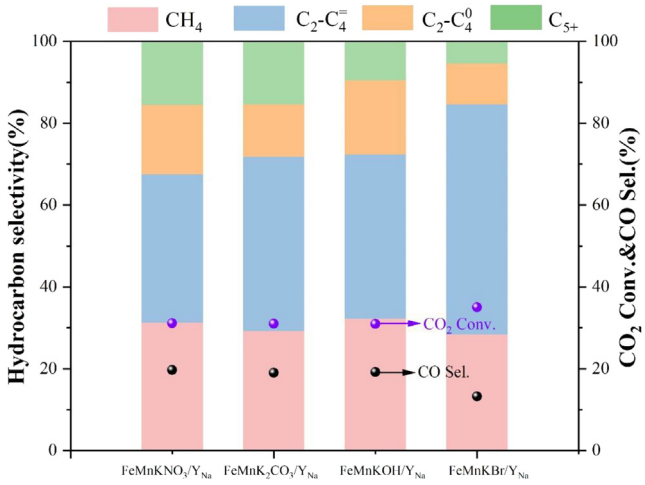

Figure 7. Catalytic performances for CO_2 hydrogenation over FeMnK/Y_{Na} catalyst

Reaction conditions: T = 300°C, p = 1.0 MPa, SV = 2160 mL g^{-1} h^{-1}, H_2/CO_2 = 3.

catalysts demonstrated maximum efficiency in terms of CO_2 conversion and product selectivity, particularly favoring the formation of low-carbon olefins.

Upon establishing the optimal reaction conditions, we proceeded to assess the catalyst's stability via stability testing. As illustrated in Figure S12, the catalyst demonstrates outstanding stability. Between the 4th and 12th hour, there is negligible variation in the CO_2 conversion rate, the selectivity for CO. Meanwhile, the selectivity for low-carbon olefins has increased.

Conclusion

In this study, the FeMnKBr/Y_{Na} catalyst demonstrated an exceptional performance at 300°C and 1 MPa, achieving a CO_2 conversion rate of 34.4%, CO selectivity of 13.6%, and a high light olefins selectivity of 56.2%. The incorporation of Br was key to this success, as it facilitated the reduction of the iron phase, leading to an increased formation of iron-carbon species and a reduced RWGS reaction, thereby diminishing CO production. K influenced the surface alkalinity and the carbon/hydrogen ratio, enhancing the carbon-carbon coupling capacity. However, the addition of Br moderated the effects of K, reducing the electron donation to the active centers. This adjustment in electron density and hydrogen density on the surface of the active centers notably improved the selectivity for low-carbon olefins. Consequently, FeMnKBr/Y_{Na} emerged as the most effective catalyst in this study, with the highest CO_2 conversion and the lowest CO selectivity.

Limitations of the study

Although the addition of Br improved the catalytic performance of the catalyst, it was found that the content of anion was different from the theoretical value.

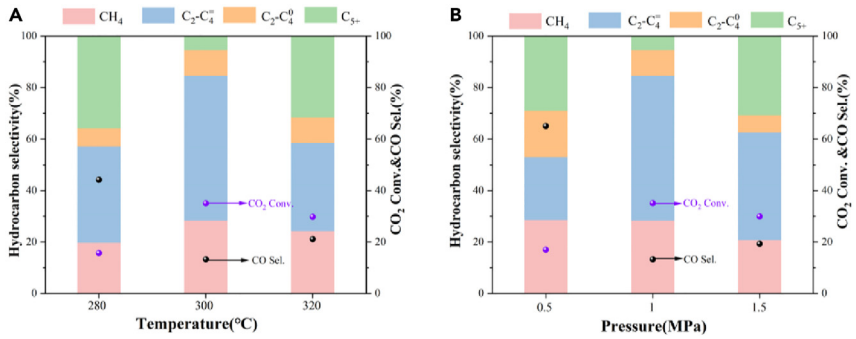

Figure 8. Temperature gradient and pressure gradient test of FeMnKBr/Y_{Na} catalyst

(A) Catalytic performances of CO_2 hydrogenation on FeMnKBr/Y_{Na} catalysts as a function of reaction temperature. Reaction conditions: p = 1.0 MPa, SV = 2160 mL g^{-1} cat^{-1}, H_2/CO_2 = 3.

(B) Catalytic performances of CO_2 hydrogenation on FeMnKBr/Y_{Na} catalysts as a function of reaction pressure. Reaction conditions: T = 300°C, SV = 2160 mL g^{-1} cat^{-1}, H_2/CO_2 = 3.

STAR★METHODS

Detailed methods are provided in the online version of this paper and include the following:

- KEY RESOURCES TABLE
- RESOURCE AVAILABILITY
  - Lead contact
  - Materials availability
  - Data and code availability
- EXPERIMENTAL MODEL AND STUDY PARTICIPANT DETAILS
- METHODS DETAILS
  - Materials
  - Catalysts preparation
  - Characterization
  - Catalytic activity tests
- QUANTIFICATION AND STATISTICAL ANALYSIS

SUPPLEMENTAL INFORMATION

Supplemental information can be found online at https://doi.org/10.1016/j.isci.2024.109621.

ACKNOWLEDGMENTS

The authors gracefully acknowledge the National Natural Science Foundation of China (22208283, 22002135, 22172032, U22A20431), Natural Science Foundation of the Jiangsu Higher Education Institutions of China (20KJB480004), and Foundation of State Key Laboratory of High-efficiency Utilization of Coal and Green Chemical Engineering (No. 2022-K49).

AUTHOR CONTRIBUTIONS

Conceptualization, J.L. and W.J.C.; methodology, J.L. and Y.D.X.; investigation, W.J.C.; writing – original draft, W.J.C., J.L., and Y.D.X.; writing – review and editing, J.L. and L.T.; funding acquisition, J.L.; resources, J.L. and P.P.Z.; data curation, W.J.C. and J.L.; formal analysis, P.P.Z., Y.J.F., X.Y., and L.T. supervision, J.L., X.Y., and L.T.

DECLARATION OF INTERESTS

The authors declare no competing interests.

Received: December 27, 2023
Revised: February 9, 2024
Accepted: March 26, 2024
Published: March 28, 2024

REFERENCES

1. Hou, Y., Li, J., Qing, M., Liu, C.-L., and Dong, W.-S. (2020). Direct synthesis of lower alkane from syngas via Fischer–Tropsch synthesis catalyzed by a dual-bed catalyst. Mol. Catal. *485*, 110824. https://doi.org/10.1016/j.mcat.2020.110824.
2. Vispute, T.P., Zhang, H., Sanna, A., Xiao, R., and Huber, G.W. (2010). Renewable Chemical Commodity Feedstocks from Integrated Catalytic Processing of Pyrolysis Oils. Science *330*, 1222–1227. https://doi.org/10.1126/science.1194218.
3. Aresta, M., Dibenedetto, A., and Angelini, A. (2014). Catalysis for the Valorization of Exhaust Carbon: from CO_2 to Chemicals, Materials, and Fuels. Technological Use of CO_2. Chem. Rev. *114*, 1709–1742. https://doi.org/10.1021/cr4002758.
4. Lorente-Vall, M., Blanco-Sans, J., Carrascón-Arconada, L., and Lozano-Compte, A. (2014). VIRTRAPP: Improving learning and knowledge retention in resuscitation application. Resuscitation *85*, S69. https://doi.org/10.1016/j.resuscitation.2014.03.174.
5. Torres Galvis, H.M., and de Jong, K.P. (2013). Catalysts for Production of Lower Olefins from Synthesis Gas: A Review. ACS Catal. *3*, 2130–2149. https://doi.org/10.1021/cs4003436.
6. Wang, G., Luo, F., Lin, L., and Zhao, F. (2021). Inverse ZnO/Cu catalysts for methanol synthesis from CO_2 hydrogenation. Reac. Kinet. Mech. Cat. *132*, 155–170. https://doi.org/10.1007/s11144-020-01919-0.
7. Yang, H., Gao, P., Zhang, C., Zhong, L., Li, X., Wang, S., Wang, H., Wei, W., and Sun, Y. (2016). Core–shell structured Cu@m-SiO_2 and Cu/ZnO@m-SiO_2 catalysts for methanol synthesis from CO_2 hydrogenation. Catal. Commun. *84*, 56–60. https://doi.org/10.1016/j.catcom.2016.06.010.
8. Jiang, F., Liu, B., Li, W., Zhang, M., Li, Z., and Liu, X. (2017). Two-dimensional graphene-directed formation of cylindrical iron carbide nanocapsules for Fischer–Tropsch synthesis. Catal. Sci. Technol. *7*, 4609–4621. https://doi.org/10.1039/c7cy01172e.
9. Xu, Y., Shi, C., Liu, B., Wang, T., Zheng, J., Li, W., Liu, D., and Liu, X. (2019). Selective production of aromatics from CO_2. Catal. Sci. Technol. *9*, 593–610. https://doi.org/10.1039/c8cy02024h.
10. Barrios, A.J., Peron, D.V., Chakkingal, A., Dugulan, A.I., Moldovan, S., Nakouri, K., Thuriot-Roukos, J., Wojcieszak, R., Thybaut, J.W., Virginie, M., and Khodakov, A.Y. (2022). Efficient Promoters and Reaction Paths in the CO_2 Hydrogenation to Light Olefins over Zirconia-Supported Iron Catalysts. ACS Catal. *12*, 3211–3225. https://doi.org/10.1021/acscatal.1c05648.
11. Dry, M.E. (2001). High quality diesel via the Fischer–Tropsch process – a review. J. Chem. Technol. Biotechnol. *77*, 43–50. https://doi.org/10.1002/jctb.527.
12. Numpilai, T., Cheng, C.K., Limtrakul, J., and Witoon, T. (2021). Recent advances in light olefins production from catalytic

hydrogenation of carbon dioxide. Process Saf. Environ. Protect. *151*, 401–427. https://doi.org/10.1016/j.psep.2021.05.025.

13. Di, Z., Zhao, T., Feng, X., and Luo, M. (2018). A Newly Designed Core-Shell-Like Zeolite Capsule Catalyst for Synthesis of Light Olefins from Syngas via Fischer–Tropsch Synthesis Reaction. Catal. Letters *149*, 441–448. https://doi.org/10.1007/s10562-018-2624-9.
14. Visconti, C.G., Martinelli, M., Falbo, L., Infantes-Molina, A., Lietti, L., Forzatti, P., Iaquaniello, G., Palo, E., Picutti, B., and Brignoli, F. (2017). CO_2 hydrogenation to lower olefins on a high surface area K-promoted bulk Fe-catalyst. Appl. Catal. B Environ. *200*, 530–542. https://doi.org/10.1016/j.apcatb.2016.07.047.
15. Witoon, T., Numpilai, T., Nueangnoraj, K., Cheng, C.K., Chareonpanich, M., and Limtrakul, J. (2022). Light olefins synthesis from CO_2 hydrogenation over mixed Fe–Co–K supported on micro-mesoporous carbon catalysts. Int. J. Hydrogen Energy *47*, 42185–42199. https://doi.org/10.1016/j.ijhydene.2021.10.265.
16. Ghosh, I.K., Iqbal, Z., van Heerden, T., van Steen, E., and Bordoloi, A. (2021). Insights into the unusual role of chlorine in product selectivity for direct hydrogenation of CO/CO_2 to short-chain olefins. Chem. Eng. J. *413*, 127424. https://doi.org/10.1016/j.cej.2020.127424.
17. Han, Y., Fang, C., Ji, X., Wei, J., Ge, Q., and Sun, J. (2020). Interfacing with Carbonaceous Potassium Promoters Boosts Catalytic CO_2 Hydrogenation of Iron. ACS Catal. *10*, 12098–12108. https://doi.org/10.1021/acscatal.0c03215.
18. Lin, B., Qi, Y., Guo, Y., Lin, J., and Ni, J. (2015). Effect of potassium precursors on the thermal stability of K-promoted Ru/carbon catalysts for ammonia synthesis. Catal. Sci. Technol. *5*, 2829–2838. https://doi.org/10.1039/c5cy00014a.
19. Zhang, P., Yan, J., Han, F., Qiao, X., Guan, Q., and Li, W. (2022). Controllable assembly of Fe_3O_4–Fe_3C@MC by in situ doping of Mn for CO_2 selective hydrogenation to light olefins. Catal. Sci. Technol. *12*, 2360–2368. https://doi.org/10.1039/d2cy00173j.
20. Chaipraditgul, N., Numpilai, T., Kui Cheng, C., Siri-Nguan, N., Sornchamni, T., Wattanakit, C., Limtrakul, J., and Witoon, T. (2021). Tuning interaction of surface-adsorbed species over Fe/K-Al_2O_3 modified with transition metals (Cu, Mn, V, Zn or Co) on light olefins production from CO_2 hydrogenation. Fuel *283*, 119248. https://doi.org/10.1016/j.fuel.2020.119248.
21. Al-Sayari, S.A. (2014). Catalytic conversion of syngas to olefins over Mn–Fe catalysts. Ceram. Int. *40*, 723–728. https://doi.org/10.1016/j.ceramint.2013.06.061.
22. Numpilai, T., Chanlek, N., Poo-Arporn, Y., Cheng, C.K., Siri-Nguan, N., Sornchamni, T., Chareonpanich, M., Kongkachuichay, P., Yigit, N., Rupprechter, G., et al. (2020). Tuning Interactions of Surface-adsorbed Species over Fe−Co/K−Al_2O_3 Catalyst by Different K Contents: Selective CO_2 Hydrogenation to Light Olefins. ChemCatChem *12*, 3306–3320. https://doi.org/10.1002/cctc.202000347.
23. Satthawong, R., Koizumi, N., Song, C., and Prasassarakich, P. (2015). Light olefin synthesis from CO_2 hydrogenation over K-promoted Fe–Co bimetallic catalysts. Catal. Today *251*, 34–40. https://doi.org/10.1016/j.cattod.2015.01.011.
24. Wang, X., Wu, D., Zhang, J., Gao, X., Ma, Q., Fan, S., and Zhao, T.-S. (2019). Highly selective conversion of CO_2 to light olefins via Fischer-Tropsch synthesis over stable layered K–Fe–Ti catalysts. Appl. Catal. Gen. *573*, 32–40. https://doi.org/10.1016/j.apcata.2019.01.005.
25. Duan, X., Wang, D., Qian, G., Walmsley, J.C., Holmen, A., Chen, D., and Zhou, X. (2016). Fabrication of K-promoted iron/carbon nanotubes composite catalysts for the Fischer–Tropsch synthesis of lower olefins. J. Energy Chem. *25*, 311–317. https://doi.org/10.1016/j.jechem.2016.01.003.
26. Wang, S., Ji, Y., Liu, X., Yan, S., Xie, S., Pei, Y., Li, H., Qiao, M., and Zong, B. (2022). Potassium as a Versatile Promoter to Tailor the Distribution of the Olefins in CO_2 Hydrogenation over Iron-Based Catalyst. ChemCatChem *14*. https://doi.org/10.1002/cctc.202101535.
27. Chen, B., Zhang, X., Chen, W., Wang, D., Song, N., Qian, G., Duan, X., Yang, J., Chen, D., Yuan, W., and Zhou, X. (2018). Tailoring of Fe/MnK-CNTs Composite Catalysts for the Fischer–Tropsch Synthesis of Lower Olefins from Syngas. Ind. Eng. Chem. Res. *57*, 11554–11560. https://doi.org/10.1021/acs.iecr.8b01795.
28. Zhang, J.-l., Ma, L.-h., Fan, S.-b., Zhao, T.-S., and Sun, Y.-h. (2013). Synthesis of light olefins from CO hydrogenation over Fe–Mn catalysts: Effect of carburization pretreatment. Fuel *109*, 116–123. https://doi.org/10.1016/j.fuel.2012.12.081.
29. Kang, S.-H., Bae, J.W., Woo, K.-J., Sai Prasad, P.S., and Jun, K.-W. (2010). ZSM-5 supported iron catalysts for Fischer–Tropsch production of light olefin. Fuel Process. Technol. *91*, 399–403. https://doi.org/10.1016/j.fuproc.2009.05.023.
30. Liang, B., Sun, T., Ma, J., Duan, H., Li, L., Yang, X., Zhang, Y., Su, X., Huang, Y., and Zhang, T. (2019). Mn decorated Na/Fe catalysts for CO2 hydrogenation to light olefins. Catal. Sci. Technol. *9*, 456–464. https://doi.org/10.1039/c8cy02275e.
31. Wang, X., Zeng, C., Gong, N., Zhang, T., Wu, Y., Zhang, J., Song, F., Yang, G., and Tan, Y. (2021). Effective Suppression of CO Selectivity for CO_2 Hydrogenation to High-Quality Gasoline. ACS Catal. *11*, 1528–1547. https://doi.org/10.1021/acscatal.0c04155.
32. Ma, W., Jacobs, G., Thomas, G.A., Shafer, W.D., Sparks, D.E., Hamdeh, H.H., and Davis, B.H. (2015). Fischer–Tropsch Synthesis: Effects of Hydrohalic Acids in Syngas on a Precipitated Iron Catalyst. ACS Catal. *5*, 3124–3136. https://doi.org/10.1021/acscatal.5b00023.
33. Dolsiririttigul, N., Numpilai, T., Faungnawakij, K., Chareonpanich, M., Rupprechter, G., and Witoon, T. (2024). Unraveling the complex interactions between structural features and reactivity of iron-based catalysts across various supports in the synthesis of light olefins from syngas. Chem. Eng. J. *480*, 148196. https://doi.org/10.1016/j.cej.2023.148196.
34. O'Byrne, J.P., Owen, R.E., Minett, D.R., Pascu, S.I., Plucinski, P.K., Jones, M.D., and Mattia, D. (2013). High CO_2 and CO conversion to hydrocarbons using bridged Fe nanoparticles on carbon nanotubes. Catal. Sci. Technol. *3*, 1202. https://doi.org/10.1039/c3cy20854k.
35. Li, J., He, Y., Tan, L., Zhang, P., Peng, X., Oruganti, A., Yang, G., Abe, H., Wang, Y., and Tsubaki, N. (2018). Integrated tuneable synthesis of liquid fuels via Fischer–Tropsch technology. Nat. Catal. *1*, 787–793. https://doi.org/10.1038/s41929-018-0144-z.
36. Kangvansura, P., Chew, L.M., Saengsui, W., Santawaja, P., Poo-arporn, Y., Muhler, M., Schulz, H., and Worayingyong, A. (2016). Product distribution of CO_2 hydrogenation by K- and Mn-promoted Fe catalysts supported on N -functionalized carbon nanotubes. Catal. Today *275*, 59–65. https://doi.org/10.1016/j.cattod.2016.02.045.
37. Huang, S., Liu, C., Chen, Y., Hong, J., Zhao, Y., Zhang, Y., and Li, J. (2020). The effect of Mn on the performance of MCF-supported highly dispersed iron catalysts for Fischer–Tropsch synthesis. Catal. Sci. Technol. *10*, 502–509. https://doi.org/10.1039/c9cy02140j.
38. Herranz, T., Rojas, S., Pérez-Alonso, F., Ojeda, M., Terreros, P., and Fierro, J.L.G. (2006). Hydrogenation of carbon oxides over promoted Fe-Mn catalysts prepared by the microemulsion methodology. Appl. Catal. Gen. *311*, 66–75. https://doi.org/10.1016/j.apcata.2006.06.007.
39. Satthawong, R., Koizumi, N., Song, C., and Prasassarakich, P. (2013). Bimetallic Fe–Co catalysts for CO_2 hydrogenation to higher hydrocarbons. J. CO_2 Util. *3–4*, 102–106. https://doi.org/10.1016/j.jcou.2013.10.002.

STAR★METHODS

KEY RESOURCES TABLE

REAGENT or RESOURCE	SOURCE	IDENTIFIER
Chemicals, peptides, and recombinant proteins		
Fe(NO3)3·9H2O	China National Pharmaceutical Group Corporation	N/A
Mn(NO3)2·4H2O	China National Pharmaceutical Group Corporation	N/A
KBr	Shanghai McLean Biochemical Technology Co.Ltd	N/A
Ymicro-Na	Shanghai McLean Biochemical Technology Co.Ltd	N/A
KNO3	Shanghai McLean Biochemical Technology Co.Ltd	N/A
KOH	Shanghai McLean Biochemical Technology Co.Ltd	N/A

RESOURCE AVAILABILITY

Lead contact

Further information, requests, and inquiries should be directed to and will be fulfilled by the Lead Contact, Li Tan (tan@fzu.edu.cn).

Materials availability

This study did not generate new unique reagents.

Data and code availability

- This study did not generate a new code.
- The information in this paper includes all the data sets generated and analyzed in this study.
- Any additional information required to reanalyze the data reported in this paper is available from the lead contact upon request.

EXPERIMENTAL MODEL AND STUDY PARTICIPANT DETAILS

This research content uses the classical Fischer-Tropsch Synthes model.

METHODS DETAILS

Materials

Iron (III) nitrate nonahydrate ($Fe(NO_3)_3·9H_2O$) and manganese(II) nitrate tetrahydrate ($Mn(NO_3)_2·4H_2O$) were purchased from China National Pharmaceutical Group Corporation. Potassium bromide (KBr) and Y_{micro}-Na (Si/Al = 5) were obtained from Shanghai McLean Biochemical Technology Co.Ltd. Further purification was not required.

Catalysts preparation

The FeMnK series catalysts were synthesized through a fusion infiltration method, with a metal weight ratio of Fe:Mn:K = 3:1:2. The detailed procedure is as follows: Initially, Y_{micro}-Na was processed to obtain Y_{meso}-Na. Typically, 6.7 g of Y_{micro}-Na and an aqueous solution of ethylenediamine-tetraacetic acid (100 mL, 0.07 mol L^{-1}) were added to the flask. The mixture was refluxed and stirred at 100°C for 6 h. The solid product was filtered and dried for subsequent NaOH treatment. For NaOH treatment, 1.7 g of solid powder was added to an aqueous NaOH solution (50 mL 0.4 mol L^{-1}), at 65°C for 0.5 h. The formation of Y_{meso}-Na was then filtered and dried.[35] Subsequently, 0.75 g of Y_{meso}-Na was meticulously ground with 1.73 g of $Fe(NO_3)_3·9H_2O$, 0.26 g of $Mn(NO_3)_2·4H_2O$, and potassium salts of different anions (KNO_3, KOH, K_2CO_3, KF, KCl, KBr, KI). The grinding continued until a moist state was achieved. The mixture was then transferred to a small sample bottle and subjected to fusion infiltration at 60°C for 48 h. Following this, the solid underwent further calcination at 550°C for 4 h under a N_2 flow of 40 mL min^{-1}, with a heating rate of 2°C min^{-1}. This process yielded the FeMnK/Y_{Na} series catalysts.

Characterization

The catalyst's X-ray diffraction (XRD) spectra were analyzed using a Bruker D8 advanced diffractometer. The analysis was conducted at a working voltage of 40 kV and current of 20 mA, utilizing monochromatic Cu Kα radiation. The angle range was set from 5 to 80° at room temperature, with a scanning speed of 2° min^{-1}.

High-resolution transmission electron microscopy (HRTEM) observations were performed using a Tecnai G2 F30 S-TWIN electron microscope. Powder samples were dispersed in ethanol through ultrasonic treatment and subsequently transferred to copper grids through impregnation.

X-ray photoelectron spectroscopy (XPS) data were obtained by an ESCALAB 250Xi electron spectrometer using 300 W Al Kα radiation. The samples were compressed into a pellet of 2 mm thickness and then mounted on a sample holder by utilizing double-sided adhesive tape for XPS analysis. The sample holder is then placed into a fast-entry airtight chamber that is not exposed to air and evacuated under vacuum conditions ($<10^{-6}$ Torr) overnight. Finally, the sample holder was transferred to the analysis chamber for XPS study. The base pressure inside the analysis chamber was usually maintained at $<10^{-10}$ Torr. The binding energies were referenced to the C 1s line of adventitious carbon at 284.8 eV

The morphology and particle size of the catalysts were studied using a field emission scanning electron microscope (SEM, S-4800, Japan). Energy-dispersive X-ray spectroscopy (EDX) was employed to detect the content of various components.

Raman spectra were recorded using a Renishaw in INVIA REFLEX Raman spectrometer with a (532 nm wavelength) Ar^+ laser and 4 mW output power. The UV-visible spectra of the catalyst samples were determined using a PerkinElmer Lambda 900 UV-Visible/NIR spectrophotometer.

Elemental composition of the catalysts was determined on an iCAP 7000 series ICP-OES (Thermo Fisher Scientific, USA).

The reduction behavior of catalysts was investigated by temperature-programmed reduction (H_2-TPR) on Micromeritics AutoChem II 2920 instrument. Before analysis, approximately 100 mg catalyst was loaded in a quartz U-tube reactor and purged with Ar at 300°C for 30 min, followed by cooling to 50°C. Then the gas stream was switched to 30 mL min^{-1} of 10% H_2/Ar, and the temperature was raised at 10°C min^{-1} to 800°C. The H_2 consumption during temperature ramp was recorded by a thermal conductivity detector (TCD).

The reduction behavior of catalysts was investigated by temperature-programmed reduction (CO-TPR) on Micromeritics AutoChem II 2920 instrument. Before analysis, approximately 100 mg catalyst was loaded in a quartz U-tube reactor and purged with Ar at 300°C for 30 min, followed by cooling to 50°C. Then the gas stream was switched to 30 mL min^{-1} of 10% CO/Ar, and the temperature was raised at 10°C min^{-1} to 800°C. The CO consumption during temperature ramp was recorded by a thermal conductivity detector (TCD).

CO_2 temperature-programmed desorption (CO_2-TPD) was conducted with similar processes. 100 mg catalyst was firstly pretreated in 20% CO/Ar at 440°C for 8 h and then cooled in He to 50°C. At 50°C, the catalyst was exposed to 10% CO_2/Ar for 30 min, followed by He purging for 60 min. Afterward, the temperature was slowly increased to 800°C and recorded the TCD signal at the same time.

NH_3 temperature-programmed desorption (NH_3-TPD) was conducted with similar processes. At 50°C, the catalyst was exposed to 10% NH_3/Ar for 30 min, followed by He purging for 60 min. Afterward, the temperature was slowly increased to 800°C and recorded the TCD signal at the same time.

Catalytic activity tests

The catalytic activity and selectivity for the hydrogenation of CO_2 to produce low-carbon olefins were assessed in a fixed-bed continuous-flow reactor equipped with an online gas chromatograph. Gas flow in the fixed-bed apparatus was regulated using mass flow controllers. In the performance testing experiment, 1.0 g of catalyst (20–40 mesh) was mixed with 2.0 g of quartz sand (20–40 mesh) and placed in the constant temperature zone of the reactor. Two temperature control detectors were installed above and below the constant temperature zone to measure the actual temperature of the reaction. Prior to the reaction, the reaction tube was pressurized with high-pressure nitrogen to check for any gas leakage issues in the fixed bed.

Carburization and reaction conditions for the catalyst were as follows: Before the reaction, the catalyst is carburized with a gas mixture of V(CO)/V(N_2) = 20%/80% (0.5 MPa and 120 mL min^{-1}) at 440°C for 8 h. After carburization, the catalyst bed was allowed to cool to room temperature. Subsequently, the feed gas (H_2/CO_2 = 3) was introduced into the reactor, and the FTS reaction was conducted under the conditions of pressure (p = 0.5–1.5 MPa), temperature (T = 280–320°C), and space velocity (GHSV = 2160 mL g^{-1} h^{-1}). To prevent the condensation of products before entering the chromatograph after exiting the reaction tube, the outlet gas path was heated using a heating tape.

The reaction products were promptly transferred to the sampling valve of an online gas chromatograph (GC-9790II) equipped with a thermal conductivity detector (TCD) and a flame ionization detector (FID) for qualitative and quantitative analysis. A TDX-01 packed column was connected to TCD, and an RB-5 capillary column was connected to FID. The packed column (2 m × 3 mm) was utilized for analyzing Ar, CO, CH_4, and CO_2, while the capillary column (50 m × 0.32 mm × 0.50 μm) was employed for analyzing all hydrocarbon products. CO_2 conversion and product selectivity (S_i) were calculated based on the internal standard method. All data were collected 4 h after the start of the reaction, unless otherwise specified.

CO_2 conversion

$$X_{CO_2} = \frac{\frac{A_{CO_2,in}}{A_{Ar,in}} - \frac{A_{CO_2,out}}{A_{Ar,out}}}{\frac{A_{CO_2,in}}{A_{Ar,in}}} \times 100\%$$

CO selectivity

$$S_{CO} = \frac{\frac{A_{CO,out} \cdot f_{CO}}{A_{Ar,out}}}{\frac{A_{CO_2,in} \cdot f_{CO_2}}{A_{Ar,in}} - \frac{A_{CO_2,out} \cdot f_{CO_2}}{A_{Ar,out}}} \times 100\%$$

$$C_i \text{ hydrocarbon selectivity}(\%) = \frac{\text{Mole of } C_i \text{hydrocarbon} \times i}{\sum_{1}^{n} \text{Mole of } C_i \text{ hydrocarbon} \times i} \times 100\%$$

QUANTIFICATION AND STATISTICAL ANALYSIS

Statistical analysis of data was performed using Excel (Microsoft) and Origin (OriginLab).